High Pressure Research
Vol. 28, No. 3, September 2008, 385–395

Taylor & Francis
Taylor & Francis Group

Combined *in situ* synchrotron X-ray diffraction and ultrasonic interferometry study of ε-FeSi at high pressure

Matthew L. Whitaker[a,b]*, Wei Liu[b], Qiong Liu[b], Liping Wang[b] and Baosheng Li[b]

[a]*Department of Geosciences, Stony Brook University, Stony Brook, NY, USA;* [b]*Mineral Physics Institute, Stony Brook University, Stony Brook, NY, USA*

(*Received 14 February 2008; final version received 4 June 2008*)

Ultrasonic interferometry was used in combination with synchrotron X-radiation to determine the compressional and shear wave velocities and unit-cell volumes of ε-FeSi (cubic B20 structure) at room temperature and pressures up to ~12 GPa. The data collected during compression are compared with those collected during decompression after heating to release stress within the sample cell. By fitting all of the decompression unit-cell volume and sound velocity data to third-order finite-strain equations, we obtain the adiabatic zero-pressure bulk and shear moduli and their first pressure derivatives: $K_{S0} = 169.3(8)$ GPa, $G_0 = 116.3(4)$ GPa, $K'_{S0} = 6.5(3)$, $G'_0 = 3.0(1)$. The bulk modulus obtained from this study is in good agreement with those of some previous experimental studies, but significantly lower than those obtained by first-principle calculations. This study presents the first direct measurement on the shear properties of this phase.

Keywords: mineral physics; ultrasonic interferometry; equation of state; iron silicide; elastic properties

1. Introduction

The composition of the Earth's core has been a longstanding question in the field of the Earth Sciences [1]. Seismic wave propagation has been used as a tool to probe the core, and inversions of these data have led to a distribution of density, compressibility and velocity profiles for the Earth's interior [2]. It has long been accepted that the core of the Earth, as well as those of other planetary bodies, is predominantly made up of metallic iron (or an iron–nickel alloy), but several studies have shown that metallic Fe is too dense to be the sole element in the core of the Earth, particularly the solid inner core [3,4]. These studies and others suggest that there must be some amount of one or more light elements in the core.

Previous investigations have suggested that silicon is a strong possibility for a light-element constituent of the Earth's core [5,6]. A recent study on several different iron-bearing phases [5] came to the conclusion that the inner core contains 2.3 wt.% Si and a trace amount of O, which accounts for the density and velocity differences between those observed for the core and pure metallic iron–nickel. There is also strong geochemical and isotopic evidence that the core of the Earth contains some amount of silicon [6].

*Corresponding author. Email: matthewlwhitaker@aim.com

ISSN 0895-7959 print/ISSN 1477-2299 online

DOI: 10.1080/08957950802246480
http://www.informaworld.com

In order to assess which elements might be present within the core of the Earth, and in what possible proportions, we must study the physical properties of various iron–light-element alloys under extreme conditions and compare them with the information obtained from seismic studies on the interior of the Earth. As silicon has been strongly suggested to be one of these elements, a clearer understanding of silicon-bearing iron alloys is necessary in order to clarify and quantify this possibility. This study focuses on one such alloy: ε-FeSi.

Under ambient conditions, FeSi occurs in the ε-FeSi form, which has a cubic B20 structure. This material has an unusual characteristic in that the coordination numbers of both silicon and iron are seven [7], and has a structure similar to the NaCl structure, but with the silicon and iron atoms displaced along the [1 1 1] directions [8]. Many studies have been conducted on this material, yet considerable debate still exists over the behavior and physical properties of ε-FeSi under extreme conditions [8–12]; in particular, there is a lack of information on the shear properties of fersilicite. This study seeks to determine the elastic properties of ε-FeSi under high pressure and examine the behavior of this material under extreme conditions by using a combination of ultrasonic interferometry and synchrotron X-radiation.

2. Experimental

The starting FeSi material was purchased in powdered form from Alfa Aesar (99.9% pure). Powder diffraction conducted on this starting material revealed that the powder was pure, homogeneous ε-FeSi in composition. This powder was then vigorously ground by hand using an agate mortar and pestle for approximately 30 min; the resulting fine powder had an average grain size on the micron scale.

This fine powder was then tightly packed into a gold capsule, dried at 150 °C for 2 h, and then the capsule was pressure-sealed to prevent adsorption of moisture. This capsule was then placed inside a standard 14/8 octahedral cell assembly and prepared for a hot-pressing experiment in a Walker-type 1000-ton uniaxial split-cylinder apparatus. The sample was sintered at 700 °C and

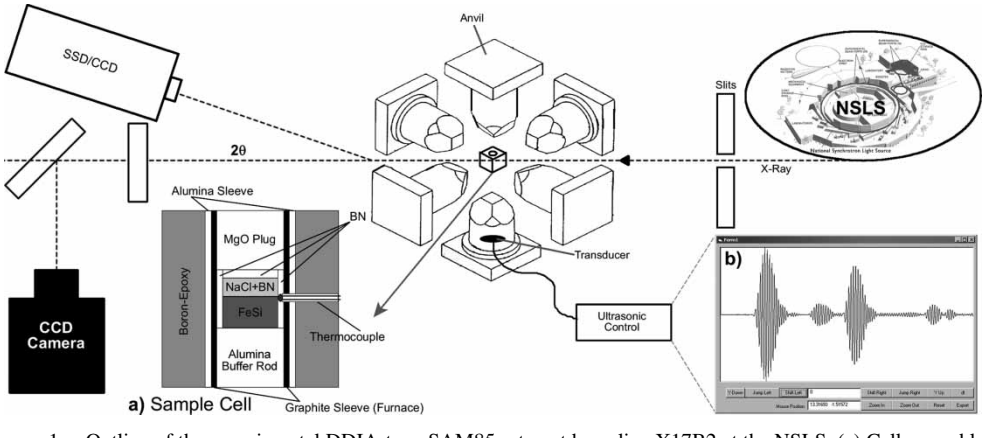

Figure 1. Outline of the experimental DDIA-type SAM85 setup at beamline X17B2 at the NSLS. (a) Cell assembly – schematic diagram of the experimental cell assembly used in this study. The NaCl + BN is a powdered mixture in 10:1 proportions; the NaCl powder serves as a pressure marker and the addition of BN to NaCl is to prevent significant grain growth of NaCl during heating. A 1-μm thick disc of Au foil is placed above and below the sample and at the bottom of the buffer rod to smooth all contact surfaces. (b) Ultrasonic interferometer – ultrasonic measurements allowing for the simultaneous collection of both P and S wave data were conducted using a dual-mode transducer capable of generating frequencies from 20 to 70 MHz. The ultrasonic signal shown here illustrates the P-wave signal collected at room temperature at 15 tons of oil pressure during initial cold compression. First pulse is anvil/buffer rod interface, second is buffer rod/sample interface and third is sample/salt interface. More information on this experimental setup can be found in [14].

7 GPa exactly for 1 h. The resulting sintered cylindrical sample was analyzed using beamline X17B2 at the National Synchrotron Light Source (NSLS) at Brookhaven National Laboratory (BNL) to check for any possible heterogeneity in composition or grain size. The sample was analyzed at ambient conditions at a series of different spots by changing its position in the beam both laterally and vertically, and the diffracted X-rays were collected by four detectors, two of which were aligned vertically and two horizontally. The diffraction patterns for each given point were virtually identical in all four detectors positioned at $\chi = 0°, 90°, 180°$ and 270°, indicating that there was no preferred orientation of grains and that grain size was homogeneous. The diffraction patterns taken at all points indicated that the sample was pure homogeneous ε-FeSi in composition.

The actual *in situ* experiment was conducted in the DDIA-type SAM85 press installed at beamline X17B2 at the NSLS. A schematic of the experimental setup is shown in Figure 1. The cell assembly used in the experiment is shown in Figure 1a. The BN capsule and the NaCl:BN

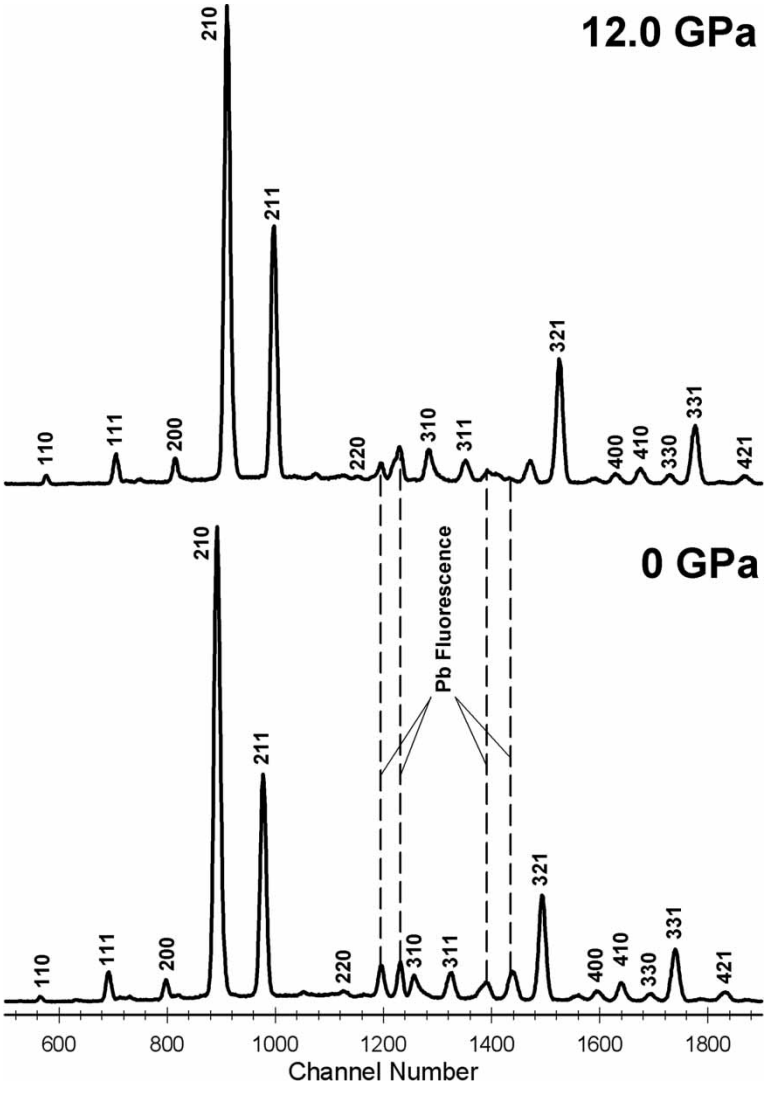

Figure 2. X-ray diffraction patterns of the sample taken at ambient pressure (bottom) and 12.0 GPa (top) at room temperature. Peaks are labeled with their *h k l* values, and Pb fluorescence peaks are shown for reference. Sample clearly remains ε-FeSi throughout the experiment. Only peaks used in cell refinement are labeled.

powder (10:1 wt.%) mixture provide a pseudohydrostatic environment for the sample. NaCl also serves as a pressure marker. To ensure that there was a minimal loss of acoustic energy at the interfaces between materials, all surfaces along the acoustic travel path were polished with 1 μm diamond paste to be perfectly flat and parallel within 0.05°; this includes the WC anvil on which the transducer was mounted, and on both sides of the buffer rod and sample. A 1-μm thick disc of gold foil was placed between the anvil and buffer rod and between the buffer rod and sample to enhance the coupling between the surfaces.

The ultrasonic measurements (Figure 1b) were conducted using a dual-mode $LiNbO_3$ transducer (10° Y-cut) that was capable of generating and receiving frequencies from 20 to 70 MHz, which allows us to determine the travel times of both P and S waves simultaneously, with a standard deviation of ∼0.2 and ∼0.4 ns, respectively. We use the transfer function method [13] to record the acoustic response of the cell assembly in the frequency range 20–70 MHz; we then extract the monochromatic waveform data from these measurements and use the pulse echo overlap technique to determine the two-way travel times of P and S waves going through the sample. In this study, P and S wave travel times are obtained at 60 and 35 MHz, respectively, for the maximum signal-to-noise ratio. An example of the ultrasonic signal for P waves at 60 MHz is shown in Figure 1b. For more information on the ultrasonic measurements and how they are processed, see [13,14].

The X-ray diffraction patterns (Figure 2) for the sample and pressure calibrants were collected in energy-dispersive mode with a solid-state Ge detector. The incident X-ray beam was collimated to 0.1 × 0.1 mm for this experiment, and the 2θ angle was calibrated to be 6.495°. The CCD camera in the experimental setup was used to record snapshot images of the cell assembly. On these images, the sample region can be identified by the contrasting brightness due to the difference in the X-ray absorption coefficients (Figure 3). This provides us a direct means of determining the length of the sample during the experiment, and the precision of this direct image measurement of sample length has been shown to be 0.2–0.4% [14].

By determining the length of the sample in pixels at the end of the experiment when the press is opened and then measuring the absolute length of the sample after the experiment, we can calibrate the pixel-to-length ratio, and thereby determine the absolute length of the sample at all

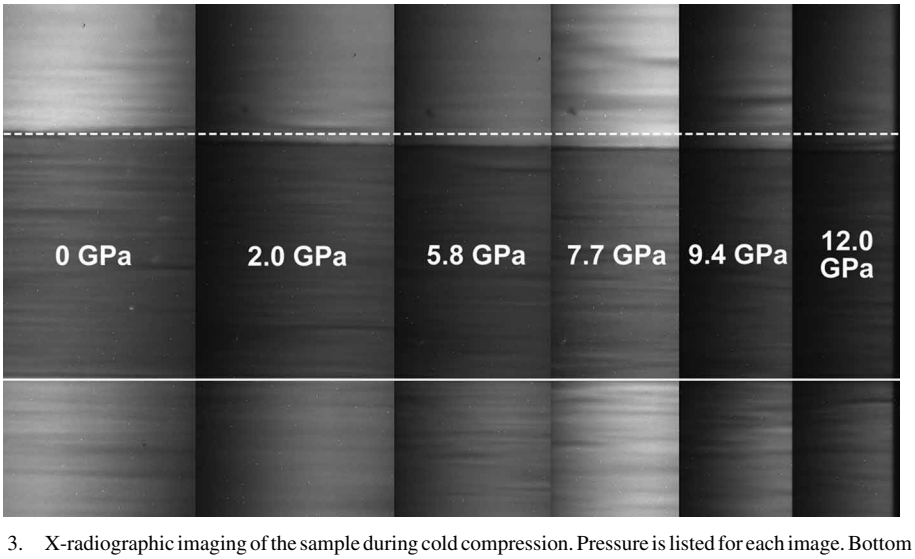

Figure 3. X-radiographic imaging of the sample during cold compression. Pressure is listed for each image. Bottom of the sample in images have been aligned to the same line and the dashed line shows top of the sample at the beginning of the experiment. Change in sample length is evident as pressure increases.

P–T conditions (Figure 3). From the lengths and travel times, we can then directly obtain the P and S wave velocities for the solid FeSi sample.

The cell assembly was placed inside the SAM85 press and brought up to the maximum oil pressure of 60 tons at room temperature T, stopping every 5 tons along the way to collect data. After the data were collected at the peak pressure, the sample was heated to a temperature of 1000 °C to relax any stress accumulated in the cell assembly during compression. After heating, the pressure was decreased systematically, and data were collected during this decompression process. After each decompression step, the sample was heated again to release any possible extensional stress acting on the system; data were collected both before and after this heating and showed good agreement between the two, which indicates that the effect of extensional stress on the system during decompression was nominally insignificant. At each desired set of conditions, an X-ray image of the sample was taken, ultrasonic data were collected, and an X-ray diffraction pattern for both the NaCl pressure calibrant and the FeSi sample were collected.

3. Results

All of the experimental data for this experiment are given in Table 1. The X-ray diffraction patterns collected during the experiment showed that the sample remained in the cubic B20 structure right up to 12 GPa, the highest pressure achieved in this study (Figure 2). Depending on the pressure

Table 1. Experimental ultrasonic and X-ray results on ε-FeSi at room temperature.

P (GPa)[a]	ρ(g cm^{-3})	$2tp$ (μs)	$2ts$ (μs)	L (mm)	V (Å^3)	V_P (km s^{-1})	V_S (km s^{-1})	K_S (GPa)	G (GPa)
2.01	6.246	0.2578	0.4304	0.9380	89.36(4)	7.28	4.36	172.7	118.7
3.35	6.293	0.2512	0.4246	0.9352	88.69(4)	7.45	4.41	186.1	122.4
4.65	6.338	0.2472	0.4202	0.9346	88.06(3)	7.56	4.45	194.9	125.5
5.79	6.376	0.2440	0.4162	0.9328	87.53(3)	7.65	4.48	202.5	128.0
6.75	6.407	0.2412	0.4122	0.9312	87.11(3)	7.72	4.52	207.3	130.9
7.72	6.438	0.2390	0.4088	0.9293	86.69(5)	7.78	4.55	212.0	133.3
8.51	6.463	0.2370	0.4056	0.9273	86.36(7)	7.83	4.57	216.3	135.0
9.42	6.490	0.2352	0.4026	0.9256	85.99(4)	7.87	4.60	218.9	137.3
10.53	6.524	0.2334	0.3998	0.9238	85.55(4)	7.92	4.62	223.6	139.3
11.40	6.549	0.2316	0.3964	0.9236	85.22(7)	7.98	4.66	227.4	142.2
11.88	6.563	0.2300	0.3950	0.9230	85.04(3)	8.03	4.67	232.3	143.1
12.02	6.567	0.2288	0.3944	0.9214	84.99(3)	8.05	4.67	234.6	143.2
5.34	6.357	0.2292	0.3898	0.8856	87.80(3)	7.73	4.54	205.1	131.0
4.80	6.339	0.2302	0.3902	0.8857	88.04(3)	7.70	4.54	201.6	130.7
4.51	6.330	0.2306	0.3894	0.8813	88.18(4)	7.64	4.53	196.3	129.9
3.91	6.310	0.2316	0.3908	0.8825	88.46(5)	7.62	4.52	194.5	128.9
3.90	6.309	0.2320	0.3916	0.8832	88.46(3)	7.61	4.51	194.3	128.3
3.18	6.285	0.2336	0.3936	0.8835	88.80(3)	7.56	4.49	190.3	126.7
3.28	6.288	0.2340	0.3946	0.8840	88.76(3)	7.56	4.48	191.1	126.2
2.90	6.275	0.2352	0.3954	0.8851	88.94(4)	7.53	4.48	187.9	125.9
2.75	6.270	0.2358	0.3964	0.8849	89.02(4)	7.51	4.46	187.3	124.7
2.32	6.255	0.2372	0.3976	0.8858	89.23(5)	7.47	4.46	183.1	124.4
1.98	6.243	0.2378	0.3986	0.8851	89.40(4)	7.44	4.44	181.5	123.1
1.82	6.237	0.2390	0.4008	0.8860	89.48(4)	7.41	4.42	180.0	121.8
1.44	6.224	0.2400	0.4024	0.8855	89.68(3)	7.38	4.40	178.3	120.5
0.74	6.198	0.2420	0.4066	0.8877	90.05(5)	7.34	4.37	176.1	118.4
0.89	6.204	0.2422	0.4070	0.8877	89.97(4)	7.33	4.36	176.1	117.9

[a]Pressures were calculated using third-order finite-strain EoS. Values in parentheses are 1σ error in the last digits. Two-way travel times have 1σ of ~0.4 ns for S waves and ~0.2 ns for P waves. The precision of image measurement of sample length is 0.2–0.4%. Uncertainties in velocities are less than 0.3%, and less than 1.0% for the derived elastic moduli. The densities at high pressures are calculated using unit-cell volumes obtained from X-ray data and the theoretical density. Top portion of data collected during cold compression (above line) and bottom portion collected during decompression after heating.

and interference from Pb fluorescence peaks, a total of 10–13 diffraction lines were used in the refinement to determine the unit-cell volume of the ε-FeSi with a relative standard deviation of less than 0.05%. Small peaks appearing in these diffraction patterns that are not labeled were either sample peaks not used for cell refinement or parasitic diffraction peaks from the surrounding material in the cell assembly.

The unit-cell volumes obtained from the refinements (using the space group $P2_13$) exhibit a smooth trend of decreasing volume with increasing pressure (Figure 4). A value of 90.45(3) Å^3 was obtained for the unit-cell volume at ambient conditions (V_0), which is slightly higher than, but comparable with, those found in previous studies on this material (Table 2). The density for each data point is derived by using the theoretical density and the unit-cell volume obtained from cell refinement at each set of conditions.

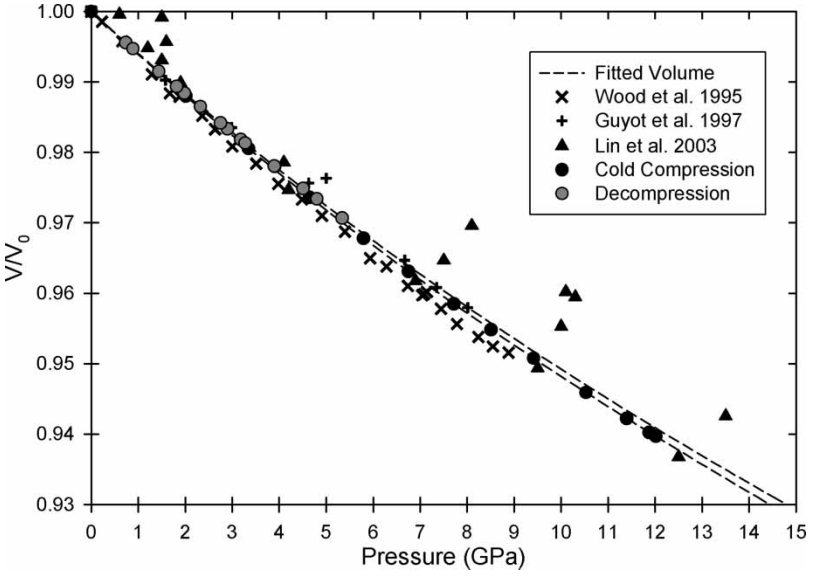

Figure 4. Variation of unit-cell volumes of ε-FeSi with pressure compared with previous studies. Crosses are the results of Wood et al. [12], plus symbols are data from Guyot et al. [9] and filled triangles are data from Lin et al. [10]. Filled circles are data collected in this study during cold compression and gray circles are data collected during decompression after heating. Dashed lines represent curves for each set of data fitted to the finite-strain equations for comparison with other data sets.

Table 2. Comparison of elastic properties of ε-FeSi with previous studies.

Ref.	P range (GPa)	K_{S0} (GPa)	K'_{S0}	K_{T0} (GPa)	K'_{T0}	V_0 (Å^3)	Method	G_0	G'_0
A	12.0	165.3(17)	6.0(3)	160.5	6.0	90.45(3)	Ultrasonics w/X-ray	113.1(8)	2.7(1)
B	**5.5**	**169.3(8)**	**6.5(3)**	**164.4**	**6.5**	**90.45(3)**	**Ultrasonics w/X-ray**	**116.3(4)**	**3.0(1)**
[11]	0	173[a]	–	–	–	–	Resonant ultrasonics	116[a]	–
[8]	50	–	–	209	3.5	89.015	XRD-DAC	–	–
[12]	9	–	–	160	4 (fixed)	90.21(2)	Neutron	–	–
[9]	8.25	–	–	172	4 (fixed)	90.39(4)	X-ray	–	–
[10]	50.7	–	–	184.7	4.75	90.193	X-ray	–	–
[18]	Calculated	227 (0 K)	3.9	227	3.9	88.896	Calculation	–	–
[19]	Calculated	–	–	255	4.143	84.09	Calculation (LDA)	–	–
[19]	Calculated	–	–	221	4.175	90.174	Calculation (GGA)	–	–

A, this study, cold compression; B: this study, decompression after heating.
[a]Estimates based on graphical data. LDA: local density approximation; GGA: generalized gradient approximation.

The adiabatic bulk ($K_S = \rho V_P^2 - 4G/3$) and shear ($G = \rho V_S^2$) moduli at high pressures are calculated from the acoustic velocities and densities. The velocity and density data are then fitted simultaneously to the third-order finite-strain equations [15] as shown below [Equations (1)–(7)] to obtain the zero-pressure elastic bulk and shear moduli and their pressure derivatives:

$$\rho V_P^2 = (1 - 2\varepsilon)^{5/2}(L_1 + L_2\varepsilon), \tag{1}$$

$$\rho V_S^2 = (1 - 2\varepsilon)^{5/2}(M_1 + M_2\varepsilon), \tag{2}$$

$$\varepsilon = \frac{1 - (V_0/V)^{2/3}}{2}, \tag{3}$$

$$M_1 = G_0, \tag{4}$$

$$M_2 = 5G_0 - 3K_{S0}G_0', \tag{5}$$

$$L_1 = K_{S0} + \frac{4G_0}{3}, \tag{6}$$

$$L_2 = 5L_1 - 3K_{S0}\left(K_{S0}' + \frac{4G_0'}{3}\right). \tag{7}$$

By fitting all of the data from the cold compression portion of the experiment, we obtain the following parameters for ε-FeSi: $K_{S0} = 165.3(17)$ GPa, $G_0 = 113.1(8)$ GPa, $K_{S0}' = 6.0(3)$, $G_0' = 2.7(1)$. Fitting the data from the post-heating decompression portion of the experiment yields slightly different results: $K_{S0} = 169.3(8)$ GPa, $G_0 = 116.3(4)$ GPa, $K_{S0}' = 6.5(3)$, $G_0' = 3.0(1)$. In order to compare the adiabatic results of this study with those of previous studies more directly, which are predominantly isothermal, we converted our data to isothermal values using the relationship $K_S/K_T = (1 + \alpha\gamma T) \approx 1.03$, where the thermal expansion coefficient $\alpha(300\,K) = 4.85 \times 10^{-5}\,K^{-1}$ and the Grüneisen parameter $\gamma = 2.33$ [16]. The pressure on the sample is then calculated directly using the Birch–Murnaghan equation

$$P(V,T) = \frac{3}{2}K_{0T}\left[\left(\frac{V_{0T}}{V}\right)^{7/3} - \left(\frac{V_{0T}}{V}\right)^{5/3}\right]\left\{1 + \frac{3}{4}(K_{0T}' - 4)\left[\left(\frac{V_{0T}}{V}\right)^{2/3} - 1\right]\right\}. \tag{8}$$

The pressures calculated in this manner are given in Table 1 and are used in the figures and discussion that follow.

4. Discussion

The iron silicide sample remained in the cubic B20 structure throughout the range of conditions explored in this experiment. First-principle calculations indicate that the transition from the B20 phase to a CsCl (B2) structure should occur anywhere from ~13 GPa [17,18] to pressures as high as 30–40 GPa [19]. Previous experimental investigations that have been conducted both in similar pressure ranges as in this study ($\leq$12 GPa) as well as to pressures above those at which the predicted phase transition occurs have also shown no sign of the B20 to B2 phase transition [5,8–10,12,20]. The first observation of the B2 structure of FeSi was not transformed from ε-FeSi, but rather synthesized from pure Fe and Si, with a slight excess of Fe in the system, at 24 GPa [21,22]. A recent study finally observed the transition from the B20 to B2 structure somewhere between 25 and 35 GPa [23]. This study, however, saw no such phase transition, as was expected.

The change in unit-cell volume with pressure is compared with the data from previous studies in Figure 4. Our data are in excellent agreement with the results of [9], and a good match with the

results of [12]. The data from [10] show a lot of scatter in the results, but a similar trend is observed in all of these data sets. It should be noted that the data presented in [10] are results of experiments conducted in diamond anvil cells, while the other two studies and this study were conducted in a multi-anvil apparatus. The data along compression and decompression from this study are essentially indistinguishable, suggesting that the deviatoric stress on the sample during cold compression is negligible. The trends followed by the compression and decompression portions of the experiment, however, are slightly different from one another, particularly with increasing pressure, reaching ~0.1% at 12 GPa, although they are considered in agreement within the current experimental uncertainties.

Figure 5 shows the variation of P and S wave velocities as a function of density along compression and those obtained during decompression, and Figure 6 displays the change in derived elastic moduli with pressure. We note that there is a slight offset in the values between data collected during cold compression and those collected during decompression after heating. As shown in Figure 4, the deviatoric stress that built up in the system during cold compression appears to be insignificant. Examination of the X-ray diffraction patterns of the sample indicate no discernable increase in the X-ray diffraction peak widths (FWHM), which also implies low stress level on the sample (quantifying the stress on the sample is impossible at present due to the lack of elastic constants data at high pressures). We therefore attribute the difference between the two data sets largely (if not all) to the further closure of porosity of high aspect ratios within the sample upon heating to 1000 °C at peak pressure. This interpretation is supported by density measurements conducted on the bulk sample before and after the current experiment using the Archimedes method. Before the NSLS experiment, the sample density was 97.9% of the theoretical density of ε-FeSi, while after the experiment, it increased to 99.1%. If this deviation from the theoretical density is taken into account, the data from both compression and decompression shown in Figure 5 would lie virtually on top of each other.

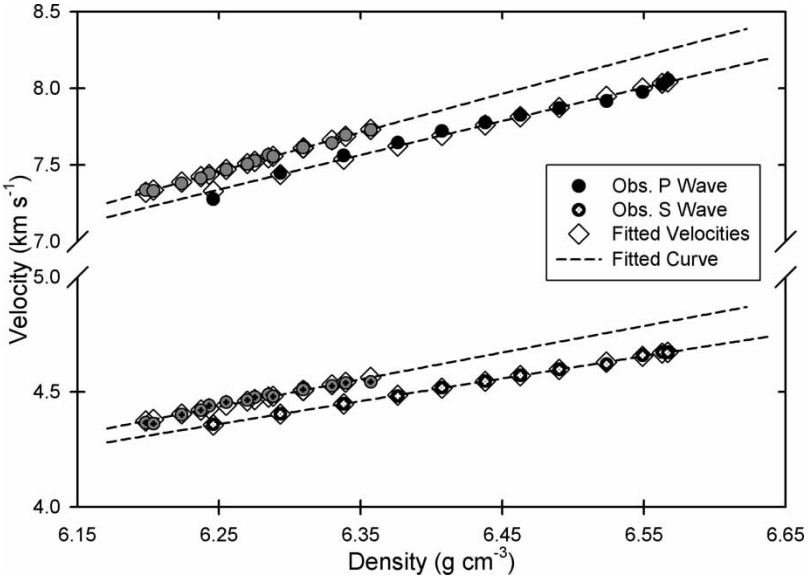

Figure 5. Variation of elastic compressional (V_P) and shear (V_S) wave velocities for ε-FeSi as a function of density from the ultrasonic measurements and X-ray data to 12.0 GPa. Solid circles are observed P wave velocities, and the circles with crosshairs represent observed S wave velocities. Filled circles are data collected during cold compression and gray circles are data collected during decompression after heating. Open diamonds are the velocities obtained from the finite-strain fitting of the elastic moduli data; dashed lines are fitted curves based on this finite-strain fitting of each data set.

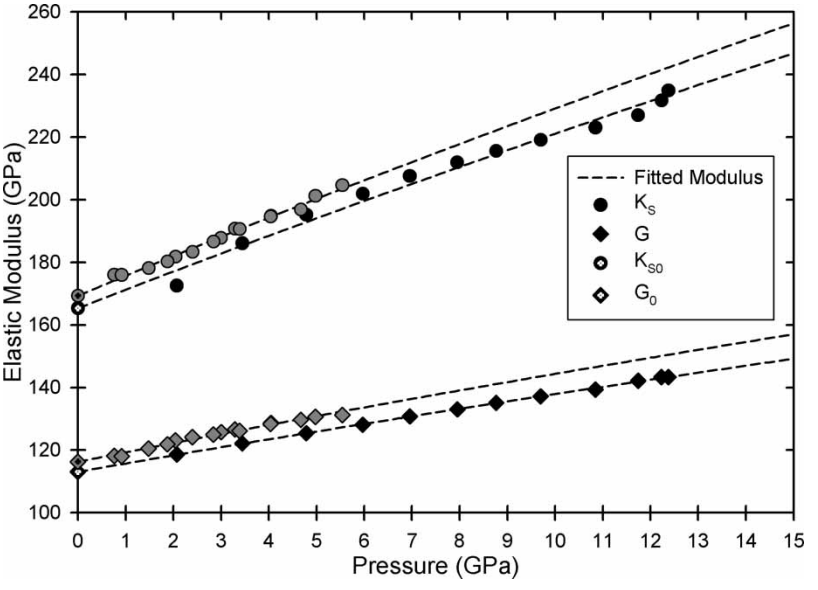

Figure 6. Variation of experimental measurements of elastic bulk (K_S) and shear (G) moduli as a function of pressure. Circles are adiabatic bulk modulus measurements and diamonds are shear modulus values. Filled symbols represent data collected during cold compression and gray symbols are those data collected during decompression after heating. Symbols with crosshairs are the zero-pressure values obtained from the finite-strain fitting of each data set. Pressures in this figure are calculated adiabatically, which accounts for the slight shift from isothermal values.

It should be noted here that a change in texture after heating the sample, if any, could also bring about changes in the observed acoustic velocities. However, in this experiment, the X-ray diffraction patterns of the sample taken both before and after heating were extremely similar in both peak position and relative intensities, which indicates that the sample did not undergo any detectable changes in grain size or orientation because of the heating. In addition, SEM images of the sample taken before and after this experiment showed no discernable differences in grain size, which indicates that little grain growth occurred.

We further note that at any given pressure, the difference in elastic moduli between the two data is on the order of $\sim$2%, and for a given density, the difference in acoustic wave velocities is $\sim$2%. This suggests that the pressure dependence obtained during compression and decompression is very similar, which is also in support for a porosity-closure origin rather than effect of stress or texture. Since the decompression data were collected under conditions that were deviatoric-stress-free within the detectability of the current experimental setup, the zero-pressure elastic moduli and their pressure derivatives calculated by fitting these data are chosen as the preferred ones for this material.

Table 2 presents a comparison of the results of this study with those of previous studies on ε-FeSi. The bulk modulus obtained from this study is significantly lower than those reported in studies based on first-principle calculations; this is true for nearly all other experimental studies on this material as well. The previously reported experimental isothermal bulk modulus for ε-FeSi ranges from 160 to 209; our result of 164.4 falls at the lower end of this range. The value of K'_{T0} obtained from this study (6.5), however, is higher than those of previous studies (range 3.5–4.75). Our G_0 agrees extremely well with the estimate based on the graphical data of [11]; this study did not present any data on the pressure derivatives of the elastic moduli. The results presented here are the first direct measurements on the shear properties of ε-FeSi, the first complete set of data pertaining to both elastic moduli and their first pressure derivatives.

At first glance, the value of G'_0 we obtained for this material may seem abnormally high, especially when compared to the normal suite of mantle minerals. The value we obtained in this study (3.0) is quite similar to the highest value for MgO obtained in previous studies (2.2–2.9, see [24]). However, when we compare these data with the results obtained from cold compression, which spans nearly twice the pressure range as that in decompression, the resulted G'_0 and K'_{S0} are lowered to $G'_0 = 2.7(1)$ and $K'_{S0} = 6.0(3)$, respectively. However, if the cold compression data are fit only over the same pressure range as the decompression data, the resulting first pressure derivatives of the elastic moduli are nearly identical to those found from the decompression data. The current data seem to suggest that there may be a relatively strong component of second pressure derivative for K and G, however, because of the difference in acoustic velocities brought about by the collapse in porosity in the sample at high pressure and temperature, this cannot be determined for certain. We need to further expand our pressure range to verify these observations.

It is important to note that the previous studies that have fitted their data to solve for both K_{T0} and K'_{T0} simultaneously [8,10] have lower values of K'_{T0} and also obtained significantly higher values for K_{T0}. An increase in one of these parameters will lead to a decrease of the other in the fitting. If we fix our results for the shear properties and set the value of K_{T0} to be equal to those given by the previous studies, our K'_{T0} decreases significantly (even becoming negative when using the K_{T0} of 209 given by [8]). If we set our K'_{T0} to be equal to those given in previous studies, then we see an increase in our value for K_{T0}. The results of this study agree fairly well with those of [10] and extremely well with those of [9]. This study fits the data to determine not only the bulk modulus and its pressure derivative, but the shear modulus and its pressure derivative as well, leading to a more complete data set. In addition, the results are not subject to the effects of pressure calibration using an outside standard; these factors lead to very robust and internally consistent results.

The results of this study have helped to clarify some of the debate regarding the physical properties of ε-FeSi under high pressure and have provided some much needed information on the shear properties of this material. In order to more fully investigate the properties of fersilicite and its likelihood as a possible constituent of planetary cores, the temperature dependence of its physical properties must be obtained. This data is currently being processed and will offer a more complete data set regarding this important material. The results presented here provide some important new insights into this phase and provide some new constraints for refining models and calculations involving ε-FeSi and its physical properties under extreme conditions by making available the first data on the shear modulus of this phase and its first pressure derivative.

Acknowledgements

The authors gratefully acknowledge the constructive reviews of Y. Wang and one anonymous reviewer, which helped to improve this manuscript. This research is supported by NSF Grants EAR00135550 and EAR0635860 to B.L. Use of the NSLS, BNL, was supported by the US Department of Energy, Office of Science, Office of Basic Energy Sciences, under Contract No. DE-AC02-98CH10886. Use of the X17B2 beamline was supported by COMPRES, the Consortium for Materials Properties Research in Earth Sciences under NSF Cooperative Agreement EAR 01-35554 and by the Mineral Physics Institute, Stony Brook University, under MPI Publication No. 470.

References

[1] W.F. McDonough and S.S. Sun, Chem. Geol. 120 (1995), p. 223.
[2] A.M. Dziewonsky and D.L. Anderson, Phys. Earth Planet. Inter. 25 (1981), p. 297.
[3] A. Jephcoat and P. Olson, Nature 325 (1987), p. 332.
[4] H.K. Mao, J.F. Shu, G.Y. Shen, R.J. Hemley, B.S. Li, and A.K. Singh, Nature 396 (1998), p. 741.
[5] J. Badro, G. Fiquet, F. Guyot, E. Gregoryanz, F. Occelli, D. Antonangeli, and M. d'Astuto, Earth Planet. Sci. Lett. 254 (2007), p. 233.
[6] R.B. Georg, A.N. Halliday, E.A. Schauble, and B.C. Reynolds, Nature 447 (2007), p. 1102.

[7] L. Pauling and A.M. Soldate, Acta Crystallogr. 1 (1948), p. 212.
[8] E. Knittle and Q. Williams, Geophys. Res. Lett. 22 (1995), p. 445.
[9] F. Guyot, J.H. Zhang, I. Martinez, J. Matas, Y. Ricard, and M. Javoy, Eur. J. Mineral. 9 (1997), p. 277.
[10] J.F. Lin, A.J. Campbell, D.L. Heinz, and G.Y. Shen, J. Geophys. Res. Solid Earth 108 (2003), p. 12.
[11] J.L. Sarrao, D. Mandrus, A. Migliori, Z. Fisk, and E. Bucher, Physica B 199 (1994), p. 478.
[12] I.G. Wood, T.D. Chaplin, W.I.F. David, S. Hull, G.D. Price, and J.N. Street, J. Phys. Condens. Matter 7 (1995), p. L475.
[13] B.S. Li, K. Chen, J. Kung, R.C. Liebermann, and D.J. Weidner, J. Phys. Condens. Matter 14 (2002), p. 11337.
[14] B.S. Li, J. Kung, and R.C. Liebermann, Phys. Earth Planet. Inter. 143–144 (2004), p. 559.
[15] G.F. Davies and A.M. Dziewonski, Phys. Earth Planet. Inter. 10 (1975), p. 336.
[16] L. Vocadlo, K.S. Knight, G.D. Price, and I.G. Wood, Phys. Chem. Miner. 29 (2002), p. 132.
[17] A.I. Al-Sharif, M. Abu-Jafar, and A. Qteish, J. Phys. Condens. Matter 13 (2001), p. 2807.
[18] L. Vocadlo, G.D. Price, and I.G. Wood, Acta Crystallogr. B Struct. Sci. 55 (1999), p. 484.
[19] R. Caracas and R. Wentzcovitch, Geophys. Res. Lett. 31 (2004), p. 4.
[20] I.G. Wood, W.I.F. David, S. Hull, and G.D. Price, J. Appl. Crystallogr. 29 (1996), p. 215.
[21] D.P. Dobson, W.A. Crichton, P. Bouvier, L. Vocadlo, and I.G. Wood, Geophys. Res. Lett. 30 (2003), p. 4.
[22] D.P. Dobson, L. Vocadlo, and I.G. Wood, Am. Miner. 87 (2002), p. 784.
[23] S. Ono, T. Kikegawa, and Y. Ohishi, Eur. J. Mineral. 19 (2007), p. 183.
[24] B.S. Li, K. Woody, and J. Kung, J. Geophys. Res. Solid Earth 111 (2006), p. 10.